Shear-induced migration and axial development of particles in channel flows of non-Brownian suspensions

G. Ovarlez, Ahmadreza Rashedi, Mohammad Sarabian, Mohammadhossein Firouznia, Dallas Roberts, Sarah Hormozi

To cite this version:

G. Ovarlez, Ahmadreza Rashedi, Mohammad Sarabian, Mohammadhossein Firouznia, Dallas Roberts, et al.. Shear-induced migration and axial development of particles in channel flows of non-Brownian suspensions. AIChE Journal, In press, ⟨10.1002/AIC.17100⟩. ⟨hal-02995438⟩

HAL Id: hal-02995438
https://hal.science/hal-02995438v1

Submitted on 9 Nov 2020

HAL is a multi-disciplinary open access archive for the deposit and dissemination of scientific research documents, whether they are published or not. The documents may come from teaching and research institutions in France or abroad, or from public or private research centers.

L'archive ouverte pluridisciplinaire **HAL**, est destinée au dépôt et à la diffusion de documents scientifiques de niveau recherche, publiés ou non, émanant des établissements d'enseignement et de recherche français ou étrangers, des laboratoires publics ou privés.

Autorisation HAL

HAL Authorization

ORIGINAL ARTICLE
TRANSPORT PHENOMENA AND FLUID MECHANICS

Shear-induced migration and axial development of particles in channel flows of non-Brownian suspensions

Ahmadreza Rashedi[1,2] | **Mohammad Sarabian**[1] |
Mohammadhossein Firouznia[1] | **Dallas Roberts**[1] |
Guillaume Ovarlez[2] | **Sarah Hormozi**[1,3]

[1] Mechanical Engineering, Ohio University, Athens, Ohio, 45701, USA

[2] University of Bordeaux, CNRS, Solvay, LOF, UMR 5258, 33608 Pessac, France

[3] Robert Frederick Smith School of Chemical and Biomolecular Engineering, Cornell University, Ithaca, NY, 14853, USA

Correspondence
Sarah Hormozi
Email: hormozi@cornell.edu

Funding information
NSF (Grant no. CBET-1554044-CAREER), ACS PRF (Grant no. 55661-DNI9) and ANR (Grant no. ANR-10–IDEX-03-02)

We present an experimental study on the shear-induced migration and axial development of particles in the channel flows of non-Brownian suspensions. The suspending fluid is Newtonian. We investigate fracturing flows with a Hele-Shaw type scaling through building a unique channel setup and an advanced optical system. The local particle concentration profiles are measured via the refractive-index matching technique for a wide range of bulk volume fraction, i.e, $0.1 \le \bar{\phi}_b \le 0.5$. Simultaneously, the particle image velocimetry is performed to determine the velocity profile of the particle phase. We compare our experimental results with the available two-phase continuum frameworks and show discrepancies and similarirties in the fully-developed and axial development of the solid volume fraction profiles. We discuss directions in which the continuum frameworks require improvements.

KEYWORDS
Non-Brownian suspensions, Fracturing flows, Shear-induced migration

1 | INTRODUCTION

Slurries are suspensions of particles in a viscous liquid. They are found in natural settings, such as landslides, mudslides, and submarine avalanches, and industrial settings, such as in petroleum industries and tailings from mining operations. In all of these examples, the dispersion of solids affect the rheology and consequently, the flow dynamics. The objective of this study is to provide experimental data on the shear-induced solid inhomogeneities in flow scenarios with the Hele-Shaw and thin-film type scalings. Notably, our focus is on the fracturing flows of non-Brownian suspensions of Newtonian fluids, for which thermal fluctuations are negligible.

The United States (US) is the largest producer of natural gas and oil. Around 50% of the oil and natural gas production in the US is the outcome of hydraulic fracturing [1, 2]. Improving fracturing techniques to enhance oil and gas production is therefore of considerable industrial and economic interest. In hydraulic fracturing, a suspension consisting of sand particles (proppant) and a viscous liquid is engineered [3]. Sometimes fractures are created in the reservoir via an explosion [4]. Then, the fractures are kept open by pumping the suspension with a high pressure all the way from the well to the fracture. The flow in the well is usually turbulent, and it becomes laminar as it divides into many branches of fractures. The grains will support the fracture when the pumping is stopped [3]. This method increases the permeability of the oil reservoir and consequently, the hydrocarbon's production. It is essential to understand the physical mechanisms underlying the dispersion of solids in fracturing flows to design new fracturing techniques and modify pumping schedules to achieve the maximum efficiency of the reservoir.

One of the recent fracturing methods that results in infinite reservoir conductivity is called the Channel Fracturing Technique (CFT) [3]. The concept behind this technology is to substitute the uniformly distributed grains of proppant (i.e., porous media) in the fracture by discrete pillars/slugs of proppant. Therefore, in CFT the reservoir fluids flow through open channels held by proppant pillars instead of porous media as in conventional fracturing methods. It is known that the effective permeability of an open channel is much higher than that of a porous medium [3]. Therefore, the proper design of this technique to achieve the open channel configuration revolutionizes the fracturing industries. We have recently provided a mathematical framework to estimate the axial dispersion of solids in CFT [5]. We showed that, to the leading order, the axial dispersion of the particle phase depends on the transverse distribution of the particles across the fracture induced by the shear. The phenomenon is called shear-induced migration, with a rich history of research that is explained in several papers [6, 7]. Nonetheless, we provide a brief review here.

In particulate flows, the particles' distribution can be attributed to the hydrodynamics and multi-body interactions of the particles. In a non-homogeneous shear flow of Newtonian suspensions, it is observed that particles migrate from the high shear rate region to the low shear rate region [8, 9], i.e., shear-induced migration. For pressure driven flows, particle migration from walls (zones of high shear rate) towards the center (low shear rate regions) has been observed by many researchers using different experimental techniques, such as Nuclear Magnetic Resonance (NMR) imaging, Laser-Doppler Velocimetry (LDV) and Refractive Index Matching (RIM). Studies extend to boundary driven flows. In summary, several experimental measurements have been carried out in different configurations, such as cylindrical Couette cells [10, 8, 9, 11, 12, 13, 14, 15, 16], pipes [17, 18, 19, 20], channels [21, 22] and two parallel disks [13, 15, 23]. By and large, the results demonstrate the migration of particles from the regions of higher shear rate to the regions of low shear rate.

Several modeling and computational approaches have been taken to explain the shear-induced migration of particles. On the computational front, techniques such as Stokesian Dynamics (SD) , Force Coupling Method and Immersed Boundary Method (IBM) are used to provide understanding of the particles' distribution and its connection with the hydrodynamics and multi-body interactions. For more information about the details of these numerical approaches, the reader is referred to the following recent work [10, 24, 25, 26, 27]. On the modeling front, at least two approaches have been taken to explain the shear-induced migration. The approach of Acrivos et al. [8, 9] is essentially phenomenological in adding a diffusive term to the right-hand side of the continuity equation for solid phase continuum. The physical origin of this term is stochastic, meaning that different initial configurations of particles will result in different evolutions. The diffusive fluxes are induced by collisions, gradients in the relative viscosity of the suspension with respect to the solid volume fraction and Brownian motion (negligible for the fracturing flows that we consider).

Another approach has effectively been made that diffusive fluxes arise naturally from gradients in the stresses associated with the particle phase, which enter the solid phase continuity equation directly by considering the particle drag closure. This is the approach underlying the Suspension Balance Model (SBM) of Brady and co-workers [28, 29, 30]. There exists rheological laws, constants and multipliers in any proposed theoretical or computational framework that should be determined from experimental measurements.

Recent advancement of the experimental techniques allowed researchers to provide well-resolved data on the distribution of particles in different shearing flow scenarios [10, 16, 20, 31]. Besides, new measurements of particle-phase stresses are provided to the community, e.g., [32, 33, 34, 35]. We refer the reader to the recent review by Guazzelli and Pouliquen [6]. Moreover, due to the improvement of computational methods [36, 24, 25, 26], interface-resolved simulations of solid particles in Newtonian fluids revealed details of the underlying physics in suspension flows. In summary, it has been shown that the recent computational and experimental data can not fully be explained by the available model frameworks [8, 9, 30]. Our recent effort in understanding the fracturing flows [5] has led us to contribute to the field [10, 37, 38, 39, 40, 41]. This paper aims to add to the existing literature by providing well-resolved experimental data on the shear-induced migration and axial development of particles in channel flows of non-Brownian suspensions. This study, along with other recent data in the field, may serve as a basis for improving and refining available model frameworks for non-Brownian suspensions.

The main, novel contributions of our study are as follows. First, we briefly explain fracturing flows of Newtonian suspensions (section 2). We design and build a unique setup with an optical system to measure the velocity and solid volume fraction profiles in channel flows of non-Brownian suspensions (section 3). Second, we provide systematic measurements of the shear-induced migration of particles and the axial development of the solid volume fraction in the channel setup for both dilute and dense suspension flows (section 4). We summarize our results and discuss the difference between our data and the prediction of the available model frameworks (section 5).

2 | CHANNEL FLOWS OF STOKESIAN SUSPENSIONS

The present work is mainly experimental. However, we use the SBM model framework with a significant simplification over a fully three-dimensional problem to build the experimental setup and design the experimental matrix. The purpose is to estimate Stokesian flows in long and thin fractures. Here, we briefly explain the SBM model framework for our channel setup and analyze one of the simplifications. As far as a detailed review of the SBM framework is concerned, we refer the reader to the recent literature [6, 5, 10, 20].

2.1 | Designing a channel for migration experiments

The objective is to build a channel that resembles a thin and long fracture in an oil reservoir (typically the length to the width ratio is beyond 1000) and to tune the fracturing suspension properties and the flow for the two-phase continuum framework to be held. Therefore, we require enough particles across the gap. Several dimensionless numbers are taken into account for scaling purposes. We study Stokesian suspensions, and we conduct experiments with negligible inertial effects at flow and particle scales.

We denote the ratio between the particle diameter ($\hat{d_p}$) and the channel gap ($\hat{D}$) by δ_p, which is of the order of (10^{-2}) to make sure that there exist enough particles across the gap to consider the suspension as a continuum medium. Another geometrical dimensionless number is $\delta_l = \hat{D}/\hat{L}$, which shows the ratio between the gap and the length of the channel ($\hat{L}$). We build a channel with, small δ_l to resemble a fracture, assuring the concentration of solid reaches a fully-developed value. It is noteworthy to mention at least two time scales exist in this problem, i.e., the advective time scale and the diffusion time scale. The former time scale is the ratio of the channel's length to the average velocity. The diffusion time scale gives an estimate of the particles' migration across the gap, which is of the order of the average shear rate times the square particle diameter. We can show that the ratio of the advective time scale to the diffusion time scale is δ_l/δ_p^2, and it is of the order of 1 in our channel, assuring the solid volume fraction achieves full-developed.

Finally, we choose δ_h (the ratio between the gap and the height of the channel $\hat{H}$) to be small enough. Therefore, in the channel's central region, the flow is 2D and it is not affected by the top and bottom wall boundaries. Table 1. presents the dimensions, the flow rate, and the dimensionless numbers of the channel setup. $\hat{U}_0$ is the mean velocity at the channel entrance. We follow the work of Miller and Morris [42] to simplify the SBM framework for our channel flows and use their results for the comparison. It is noteworthy to mention that solving the full 3D problem numerically is beyond this experimental work scope.

2.2 | SBM equations in a channel flow

Here, we study density-matched Stokesian suspensions. Therefore, we neglect inertial and gravity effects. Below, we briefly present the SBM approach explained in [42] to derive the system of equations that needs to be solved for modeling channel flows of non-Brownian suspensions.

In the suspension balance model [30, 43, 44, 45], the gradient of particle normal stress causes the diffusive flux of particles. The transport equation for the solid volume fraction ϕ is as follows [42]

$$\frac{\partial \phi}{\partial t} + \nabla \cdot [\phi \mathbf{u}] = -\nabla . [\frac{{d_p}^2}{18\eta_f} f(\phi) \nabla . \Sigma^p] \tag{1}$$

where u is the suspension velocity, Σ^p is particle stress tensor, η_f is the viscosity of the Newtonian fluid, and $f(\phi)$ is the hindrance function:

$$f(\phi) = (1 - \phi)^{\alpha} \tag{2}$$

In order to compute the distribution of the solid volume fraction, the equation 1 is solved together with the mass and momentum equation for the suspension flow:

$$\nabla . u = 0 \tag{3}$$

$$\nabla . \Sigma = 0 \tag{4}$$

where $\Sigma = \Sigma^f + \Sigma^p$ is the suspension stress tensor. The particle phase stress Σ^p and the fluid phase stresses Σ^f are:

$$\Sigma^p = -\Sigma_N^p + 2\eta_f \eta_p E \tag{5}$$

$$\Sigma^f = -P_f I + 2\eta_f E \tag{6}$$

where P_f is the pressure of the fluid phase, I is the identity tensor, E is the strain rate tensor, and Σ_N^p is the particle phase normal stress tensor which is rewritten as:

$$\Sigma_N^p = \eta_f \eta_N |\dot{\gamma}| Q \tag{7}$$

$$Q = \begin{bmatrix} 1 & 0 & 0 \\ 0 & \lambda_2 & 0 \\ 0 & 0 & \lambda_3 \end{bmatrix} \tag{8}$$

where η_N is the relative normal viscosity of the suspension, and $\eta_s = \eta_p + 1$ is the relative shear viscosity of the suspension.

These equations have been solved by Miller and Morris [42] using the finite-volume method with the rheological model proposed by Morris and Boulay [42] as a closure. The rheological laws of Morris & Boulay (1999) are:

$$\eta_N = K_n (\phi/\phi_m)^2 (1 - \phi/\phi_m)^{-2} \tag{9}$$

$$\eta_s = \eta/\eta_f = 1 + 2.5\phi(1 - \phi/\phi_m)^{-1} + K_s (\phi/\phi_m)^2 (1 - \phi/\phi_m)^{-2} \tag{10}$$

with $K_n = 0.75$, $K_s = 0.1$, $\alpha = 4$, $\lambda_2 = 0.8$, $\lambda_3 = 0.5$, and $\phi_m = 0.6$.

The results obtained for the steady-state solution by Miller and Morris [42] will be compared to our experimental results.

As discussed by Miller and Morris [42], a simplified version of the transport equation can be solved provided (i) the flow throughout the conduit is steady (meaning that $\frac{\partial \phi}{\partial t} = 0$), and (ii) the flow can be considered as 2D (i.e., variations across z can be neglected). This is precisely achieved in our experiments thanks to (i) the suspension recirculation in the channel which allows reaching a steady-state and (ii) the small width to height ratio of the channel. In these conditions, Eq. 1 finally reduces to:

$$u_x . \frac{\partial \phi}{\partial x} = -\frac{\partial}{\partial y} [\frac{{d_p}^2}{18\eta_f} f(\phi) \frac{\partial}{\partial y} \Sigma_{yy}^p] \tag{11}$$

We have solved numerically this equation together with the suspension momentum equation with the closures of Morris and Boulay [43] given above. We solve this nearly one-dimensional equation numerically. The equation is solved following Miller and Morris by computing progressively the velocity $U(y)$ when the solution marches through the channel. At each position y, $U(y)$ is computed from stress balance and from the current solution $\phi(y)$, while ensuring that the suspension flux remains constant. Note that the particle flux also remains constant. The steady-state volume fraction profiles and their axial development will be compared to the experimental results. Moreover, we also compare our experimental results with the fully 2D channel solution given by Miller and Morris [42]. It is noteworthy to mention that we compare the present work with the results of Miller and Morris [42] 2006, Figure 6 with $\dot{\gamma}_{NL} = \epsilon^2$. In the present work we have considered $\phi_m = 0.6$, and the regularization parameter as $\epsilon = 10^{-5}$.

We report our results in dimensionless form and adopt a cartesian coordinate system shown in Figure 1 (a). The axes are scaled with the dimensions of the setup, i.e., $\hat{L}, \hat{D}, \hat{H}$.

3 | METHODOLOGY

This section explains our experimental methodology. That includes the channel setup, visualization system, test fluids and particles, experimental procedure and image analysis.

3.1 | Experimental setup

As explained in section 2 (see also Table 1), a channel setup resembling a fracture requires a length that is three orders of magnitude larger than the width. The dimension requirements of the channel makes the tolerance extremely small on all dimensions. Moreover, we want to build the channel using transparent acrylic materials to be able to visualize the flow. Maintaining the tolerances while machining the acrylic (Poly methyl methacrylate (PMMA)) materials is extremely difficult. These tolerances can not be maintained on extremely long pieces of acrylic due to the variance in the stock itself. Therefore, we constructed the channel out of 20 smaller and more accurate channel sections. The length of each section is $20\ cm$. Figure 1 (b) shows one of the sections that includes 3 channels. A central channel ($2\ mm$ width) for the suspension to flow and two side channels ($3\ mm$ width) to recirculate water for controlling the temperature of the suspension and consequently its refractive index.

The sections of channel are precisely aligned and sealed together and the O-rings between the sections prevent possible leakages (see Figure 1 (c)). The setup, shown in Figure 1 (a), is then mounted on a RPR-416-12 RPR reliance optical table top purchased from Newport. The table top is 0.3048 m thick with a 1.2192 m width, a 4.8768 m length, and $M6 \times 1$ holes on a 0.0254 m grid. The S-2000A-423.5 stabilizer set was also purchased from Newport to support the table top. This stabilizer set consists of four vibration dampening legs that the table top is connected to. This set up provides a completely flat and vibration free area for the channel to sit.

We use a precision syringe pump (two high-pressure modules purchased from neMESYS GmbH) to pump the suspension in the central channel and simultaneously we recirculate water in the side channels using a water bath.

3.2 | Test particles and fluids

We make a transparent model suspension consisting of non-Brownian particles and Newtonian suspending fluids as follows. PMMA particles are used with the diameter in the range of $75 - 90 \mu m$. The density and refractive index of PMMA particles are $\rho = 1.19 gr/ml$ and $n = 1.49$ respectively. The fluid for the Newtonian suspension is similar to what Pham used [46]. It is a combination of Triton x-100(76 wt%), Zinc Chloride(14.9 wt%), water(9 wt%), and hydrochloric acid(0.1 wt%). The viscosity is 4.64 Pa.s. The weight fractions are defined in a way to match the density and refractive index (RI) of PMMA particles. To recognize PMMA particles from the fluid during the imaging, a fluorescent dye (rhodamine 6G) is mixed with the fluid phase with a concentration of 3 mg/l. The dye concentration is set to optimize the contrast between the solid and liquid phases. The temperature of the set-up is set to $30^o C \pm 0.1^o C$ in order to maximize RI matching between the solid and fluid phases (within 10^{-4}). This suspension is the same as that used by Snook et al. [20] and Sarabian et al. [10]. Sarabian et al. [10] have shown that its rheological behavior is fairly modeled by the Morris and Boulay [43] laws presented is Sec. 2.

For each experiment, we make $1300\ ml$ of the suspension and we take the following steps. First, the particles are washed using an ultrasonic water bath. Then the particles are placed in the oven at 50°C for 48 hours to ensure that they are completely dried. The particles and the fluid are mixed for 3 hours to be completely homogenized. The prepared suspension is left in a closed and sealed container (with almost no evaporation) for 24 hours to make sure the bubbles are removed.

3.3 | Experimental procedure

We pour the suspension in a reservoir very gently to avoid trapping bubbles. We load the syringe pumps with the suspension from the reservoir. The syringe pumps operate at the flow rate of $0.01\ ml/s$, draw the suspension from the reservoir, and send it to the channel. We designed a plumbing system to recirculate the suspension to the reservoir. A perforated blade is machined and placed in the reservoir to homogenize the suspension gently. The plumbing system consists of tubes and ball valves made of Polyoxymethylene material purchased from Advanced Technology products.

The circulating water bath pumps the water through the side channels and maintains the temperature at $30^oC \pm 0.1^oC$ to maximize the refractive-index matching between the solid and the fluid phases. Experiments are performed at five different bulk volume fractions of $\bar{\phi}_b = 0.1, 0.2, 0.3, 0.4$, and 0.5. We built an optical setup to scan the channel vertically by taking images from the top to the middle plane. The optical setup is mounted on a rail system and moved along the channel to scan the axial development of the flow. Section 3.4 explains the details of the optical system.

After finishing the experiment, we remove the pumps and the tubing, and we tilt the channel using two gas spring jacks. It takes about two days for the suspension to drain gradually. We collect the suspension and wash the particles with a large amount of water to remove the suspending fluid. We use an ultrasonic water bath to remove any possible residue of the suspending fluid from the particles to be able to reuse them. The channel is washed with the filtered water to remove all the residues of the suspension, and it is then air-dried for several days.

It is noteworthy to mention that the current data reported for each bulk volume fraction required about 60 days of performing an experiment, which includes preparing the materials, conducting the test, scanning the setup, draining, cleaning, and washing the setup. Scanning the setup itself included a loop of examining the quality of images, tuning the optical setup and temperature for that specific experiment, and rescanning until achieving the best quality images. These tasks exclude the time and effort of designing and building the setup and in-house optical system.

3.4 | Optical setup

We use the refractive-index matching technique to visualize the suspension flow. The optical setup is illustrated in Figure 1 (a). A semiconductor green laser diode of 200 mW power and wavelength of 532 nm is used as the light source. The laser passes through a vertical plano-convex cylindrical lens with a focal length of $(f = 10mm)$ to make a horizontal laser sheet. The diverging laser sheet goes through a vertical plano-convex cylindrical lens with a focal length of $(f = 100mm)$ to collimate the laser sheet. A horizontal plano-convex cylindrical lens with a focal length of $(f = 50mm)$ is used to thin the laser sheet thickness ($\approx 15\mu m$) [47, 48].

The suspending fluid contains rhodamine 6G, which illuminates under the laser diode projection. The concentration of rhodamine is chosen to be $3\ mg/l$ to optimize the contrast between the particles and fluid all over the gap. The fluorescent dye absorbs 524 nm (green) wavelength laser light and emits it at 566 nm. Since the suspension is trans-

TABLE 1 Experimental parameters

$\hat{L}\ [mm]$	$\hat{H}\ [mm]$	$\hat{D}\ [mm]$	$\hat{d}_p\ [mm]$	$\hat{U}_0\ [mm/s]$	$\hat{\eta}_0[Pa.s]$
4000	40	2	0.075-0.09	0.125	4.64
$\hat{\rho}_0[g/ml]$	$\delta_l = \frac{\hat{D}}{\hat{L}}$	$\delta_h = \frac{\hat{D}}{\hat{H}}$	$\delta_p = \frac{\hat{d}_p}{\hat{D}}$	$Re = \frac{\hat{\rho_f}\hat{U}_0\hat{D}}{\hat{\eta}_0}$	$Re_p = \frac{\hat{\rho_f}\hat{d}_p{}^2\hat{\dot{\gamma}}}{\hat{\eta}_0}$
1.19	5×10^{-4}	0.05	~ 0.041	6.41×10^{-5}	1.09×10^{-7}

parent, the light can go through without diffraction. A 2-megapixel CCD camera (purchased from Basler) mounted on top of the channel receives the light from the suspending fluid. A macro lens (purchased from Sigma-Photos) is mounted on the CCD camera to be able to visualize small particles of the diameter of $60\mu m$ and above. A high pass filter (550 nm filter purchased from Thorlabs) is mounted between the camera and channel to remove the noise. The particles are not covered with fluorescent dye, therefore a contrast forms between the particle phase and the fluid phase and makes it possible to visualize the suspended particles.

This optical system allows us to take high quality images of the suspension flows. The exposure time of the camera is set to be 20 ms and 100 images are taken at each location. The laser power is set to be 80% of the capacity of a 200 mW laser generator. The laser power is tuned to have enough light in the camera sensor and also avoid bleaching the dye in the fluid. A typical example of images is shown in figure 2. The images correspond to the plane located in the middle of the height of the channel. The distribution of particles at the inlet and outlet experimental windows are shown. For all of the solid volume fractions, the suspension is homogeneous at the entrance. However, at the outlet the solid volume fraction is inhomogeneous due to the migration of particles from the walls to the center of the channel.

3.5 | Image analysis

The key factors in successful computation of the local solid volume fraction are first to accurately discern each particle in the image plane, and second to retain the particle shape. In particular, the latter factor is crucial to extract the particle concentration profiles and particle velocity by the means of circular Hough transform (CHT) which was previously adopted by Sarabian et.al [10] and Snook et al. [20] respectively. In this study, we compute the solid volume fractions in several steps. First, the image contrast is enhanced to distinguish particles from the background fluid by computing several histograms, each corresponding to a separate part of the image, and uses them to redistribute the intensity values of the image. Next, a threshold was calculated which implements the Li method [49] that is an iterative method based on the minimum cross-entropy thresholding using ImageJ [50]. In this method, a threshold level is computed by minimizing the spread function from the foreground and background classes. Once the optimization procedure is over and the threshold level is found from the iterative algorithm, then we filter the image by allocating pixel intensity values smaller than the threshold level as black, and the rest as white. Figure 3 depicts typical examples of an image before and after applying the threshold at two different bulk volume fractions. The resulting image out of this step is a binary image and we can easily infer the solid volume fraction by accounting the black pixels as particles and white pixels as background fluid.

Particle Image Velocimetry (PIV) is performed to measure the particle velocity U_p from successive images recorded from the suspension flow at 0.1 s time intervals. The velocity field is calculated in the shear plane (xy plane) and then averaged in the x direction to compute the velocity profile. For more information on the PIV procedure, the readers are referred to the work of Firouznia et al. [41]. MatPIV [51] was employed to analyze the pairs of images. Each

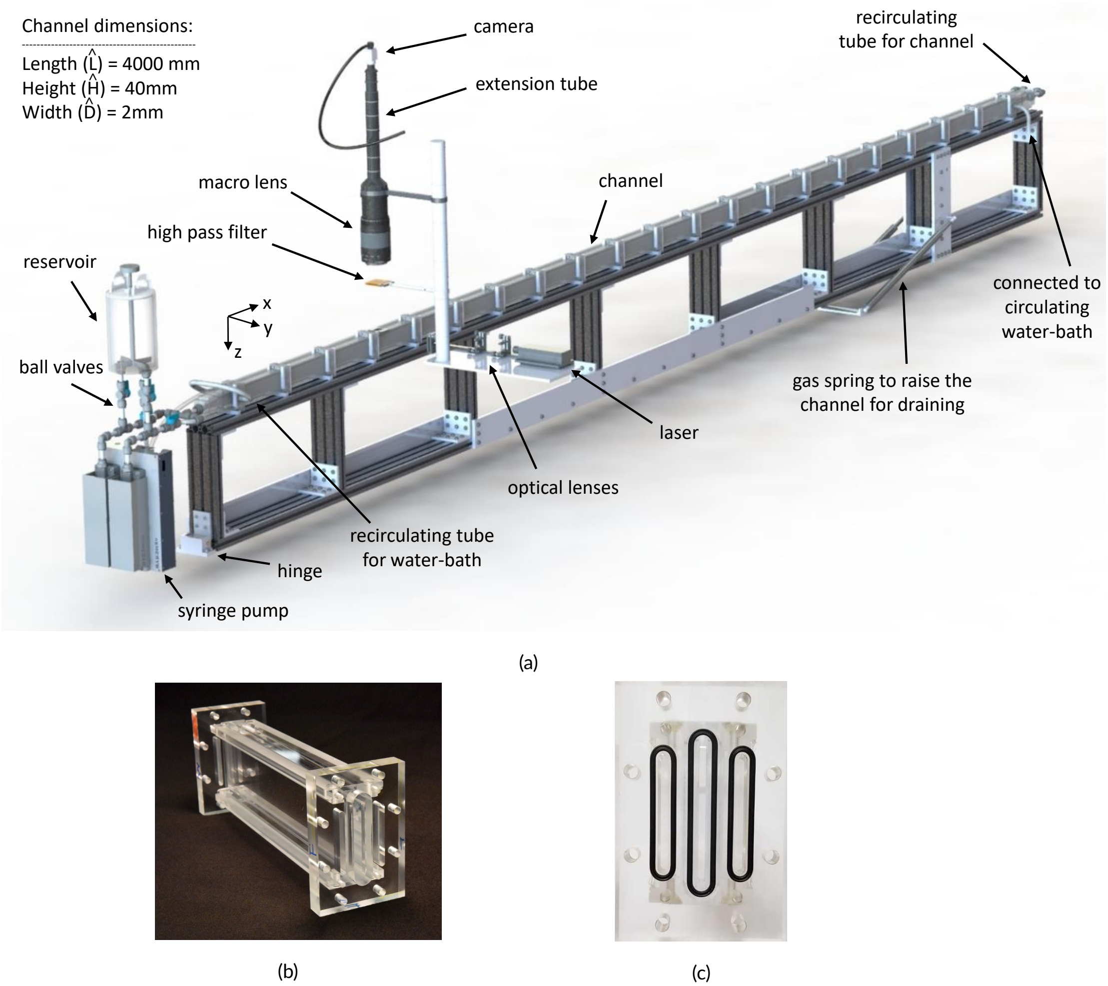

(a)

(b)

(c)

FIGURE 1 A schematic of the experimental setup; (b) A section of the channel; (c) O-rings placed at the end of each channel section for the sealing.

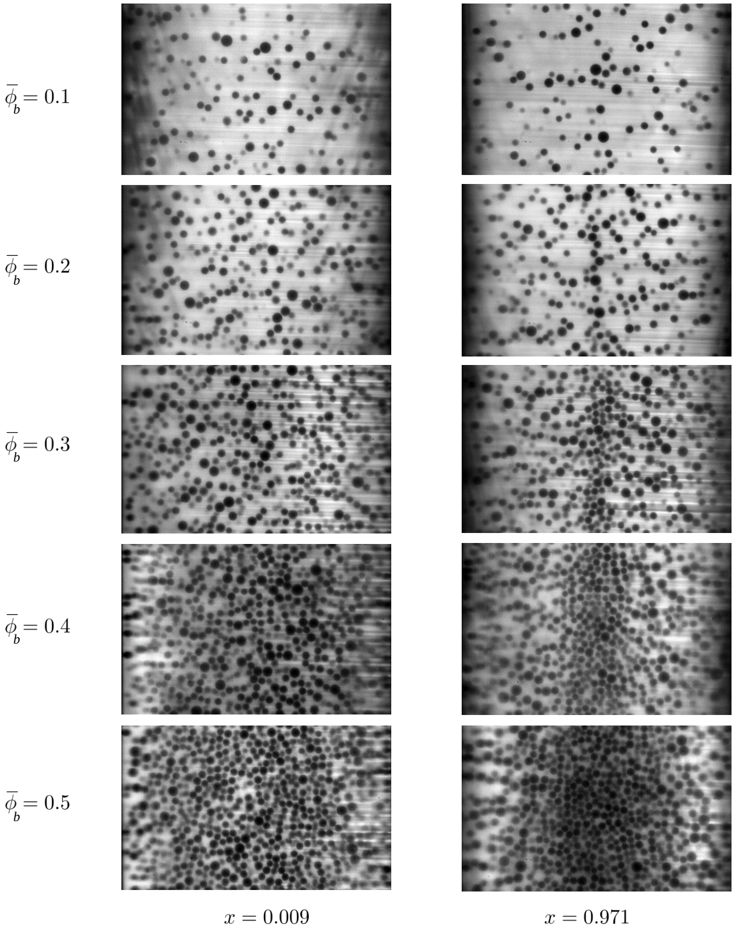

FIGURE 2 The raw images of the suspension flow at the beginning and the end of the channel setup for different bulk solid volume fractions.

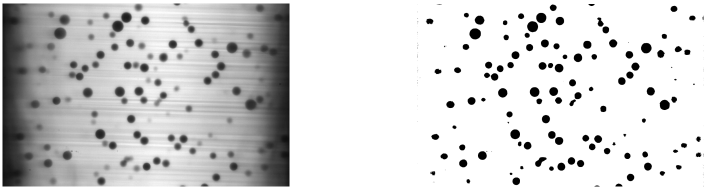

(a) $\bar{\phi}_b$ = 0.1 raw image

(b) $\bar{\phi}_b$ = 0.1 threshold

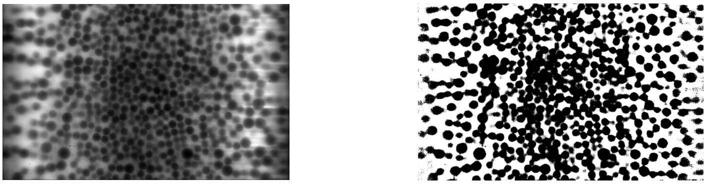

(c) $\bar{\phi}_b$ = 0.5 raw image

(d) $\bar{\phi}_b$ = 0.5 threshold

FIGURE 3 Image processing of particles suspended in the Newtonian fluid; (a) A raw image sample at $\bar{\phi}_b = 0.1$; (b) the threshold of the sample image at $\bar{\phi}_b = 0.1$; (c) the raw image sample at $\bar{\phi}_b = 0.5$; (d) the threshold of the sample image at $\bar{\phi}_b = 0.5$.

image is divided into sub-images (interrogation windows) with overlap of 50%. The PIV algorithm uses two successive images and takes the corresponding interrogation windows in order to perform cross correlation and compute the velocity field. The PIV algorithm iterates the cross correlation twice with the window sizes of 64×64 and 32×32 pixels to improve the accuracy. Several filters such as signal to noise ratio (SNR) are used to identify the false vectors. The false vectors are removed and replaced by linear interpolation between the neighboring vectors.

4 | RESULTS AND DISCUSSION

In this section, we present the experimental measurements of the velocity profile of the suspension as well as the solid volume fraction at different parts along the channel. We also compare our results with the SBM and some available experimental and computational data.

As discussed in section 2, from the small width to height ratio of our channel, the central part of the channel flow can be approximated as a 2D flow. Therefore the boundary effects in the vertical direction ($z$direction) are insignificant. We examine this point by measuring the concentration profile across the width of the channel (y direction) at different locations along the z axis. Figures 4 a & b illustrate the particle volume fraction close to the entrance ($x = 0.009$) and outlet ($x = 0.971$), respectively. The results correspond to the experiment with $\bar{\phi}_b = 0.4$.

Several features are evident. First, we note that the variation of ϕ along the vertical direction z is insignificant compared to the change of ϕ across the width y. Second, the concentration profile is symmetric around $y = 0$ due to the setup's geometrical symmetry. Therefore, we merely show our measurements in half of the width. The results validate our assertion in section 2 that the flow is 2D (in the xy plane) and the vertical boundary effects are negligible on the suspension dynamics from $z \geq 0.125$. This justifies comparing our data with the solution of the 2D SBM problem.

It is noteworthy to mention that we were unable to compute the solid volume fraction in the narrow region close to the solid walls, i.e, in $0.4 < y \leq 0.5$. However, the velocity profile of the particle phase can be measured in the

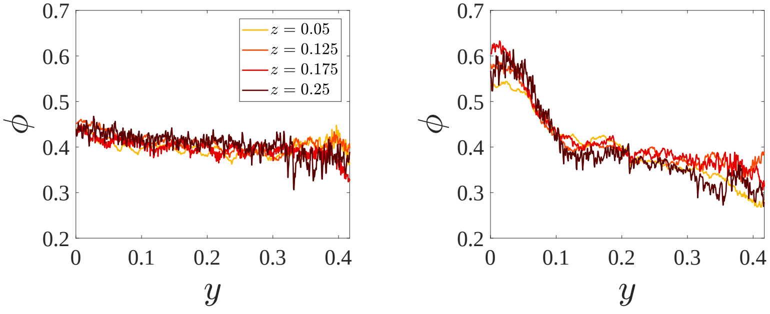

(a) entrance (x = 0.009)

(b) outlet (x = 0.971)

FIGURE 4 The particle concentration profiles at different channel's height (direction z) plotted across the gap (a) the inlet, (b) the outlet of the channel; The bulk volume fraction is $\bar{\phi}_b = 0.4$.

whole gap (shown later). The slight and invisible residue of glues used for constructing the channel affects the quality of the image. Therefore, close to the walls, there exist streaks lowering the signal-to-noise-ratio. The streaks close to the walls can be seen in the raw images shown in figure 2. Consequently, in this paper, we only report the volume fraction measurements in $0 \leq y \leq 0.4$.

Figure 5 demonstrates the particle concentration profiles at the end of the channel at different bulk volume fractions. The fully-developed concentration profiles are computed near the channel outlet, at $x = 0.971$. For all the bulk volume fractions, the concentration profiles indicate the migration of particles from the walls (high-shear-rate region) toward the channel centerline (zero-shear-rate zone). Besides, we observe that maximum particle volume fraction, which occurs at the channel centerline ($y = 0$), increases with the bulk volume fraction. For those experiments with $\bar{\phi}_b \gtrapprox 0.3$, the maximum value of ϕ is about 0.6 at the center of the channel. This behavior is consistent with the solution of equation (10). At the fully-developed state, the left hand side of the equation is zero implying that Σ_p is constant across the channel. A nonzero constant value of Σ_p at the center of the channel, where the shear rate is zero, is possible if the viscosity of the suspension diverges. This singular behavior occurs at the limit of jamming volume fraction, i.e., $\phi \rightarrow \phi_m$. Therefore, the trends of solid volume fraction profiles for $\bar{\phi}_b \gtrapprox 0.3$ follow the prediction of the dimensionless governing equations, which are based on the SBM. It has been shown that the value of ϕ_m is around 0.585 by several researchers (see e.g. [35] and Guazzelli and Pouliquen [6]). Consistently, our results show that the central value of ϕ that corresponds to the maximum packing volume fraction is about 0.6.

Another important observation is that in the dilute suspension regime, i.e, at $\bar{\phi} \lessapprox 0.3$, the value of the particle volume fraction ϕ at the channel center is less than the maximum packing fraction ϕ_m. This observation is not consistent with the prediction of the SBM and, more specifically, the solution to the equation (11). As explained above, according to the SBM, the solid volume fraction should approach ϕ_m at the center of the channel where the shear rate is zero. This prediction is independent of the value of $\bar{\phi}_b$. It is in contrast with what we observe in our experimental measurements. Indeed, based on Figure 5 (a) & (b), ϕ does not reach to ϕ_m at $y = 0$, but to a value that is an increasing function of $\bar{\phi}_b$. Recently, several other experimental observations have been reported that do not follow the SBM's prediction, calling for the theoretical and numerical studies to improve the model framework for the non-Brownian suspensions [10, 16].

Moreover, we observe that the maximum variation of ϕ across the channel occurs for the experiments with $\bar{\phi}_b \sim 0.3$. Therefore, the migration amplitude exhibits a non-monotonic behavior with the bulk volume fraction. We

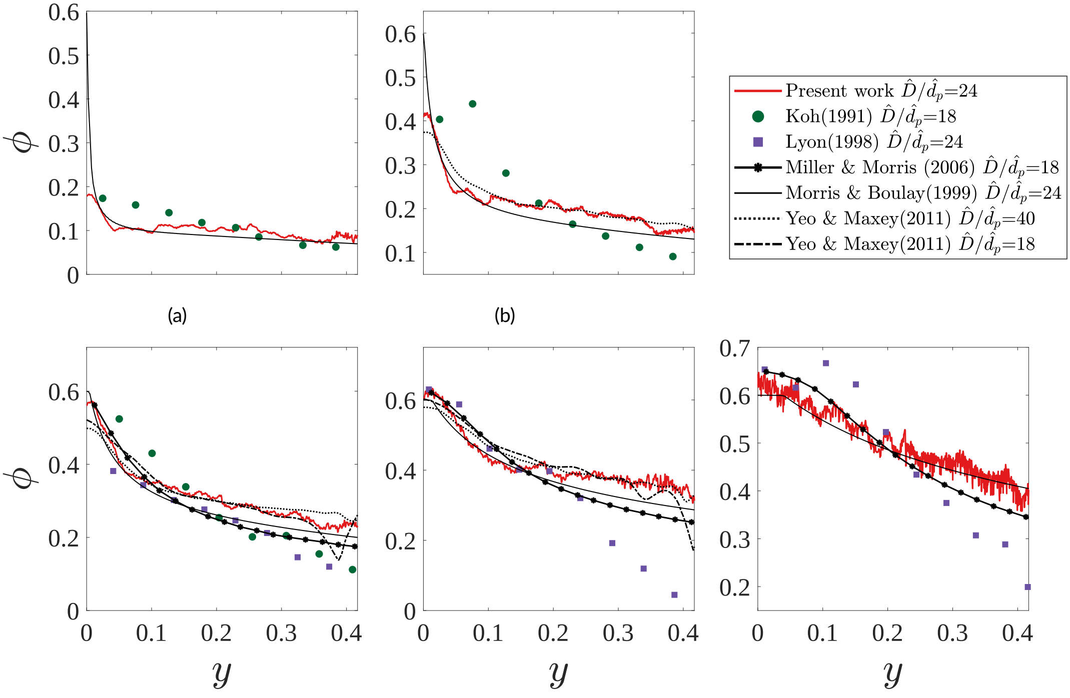

(a) (b)

(c) (d) (e)

FIGURE 5 Particle concentration profiles at the end of the channel at (a) $\bar{\phi}_b$ = 0.1, (b) $\bar{\phi}_b$ = 0.2, (c) $\bar{\phi}_b$ = 0.3, (d) $\bar{\phi}_b$ = 0.4, and (e) $\bar{\phi}_b$ = 0.5. The measurements are compared with the experimental studies of Koh *et al.* [21], Lyon & Leal [22], two dimensional SBM prediction with the rheological law of Morris & Boulay (1999) [43], three dimensional SBM results of Miller & Morris (2006) [42] , and simulations of Yeo & Maxey [36]. Note: the data of Miller & Morris [42] corresponds to Figure 6 of their paper with $\dot{\gamma}_{NL} = \epsilon^2$.

have also shown the non-monotonic trend in our recent work concerning the suspension flows in a wide-gap Taylor-Couette cell [10].

We have compared the particle concentration profiles at the end of the channel with the available experimental and computational studies in Figure 5. According to this figure, the previous experiments of Koh *et al.* [21] and Lyon & Leal [22] performed in a rectangular channel are in agreement with our measurements qualitatively in the core region, i.e, far from the walls and the center of the channel. However, the experiments of Lyon & Leal [22] at $\bar{\phi}_b$ = 0.4 fails to correctly measure the particle concentration in the vicinity of the channel wall. The discrepancy might be due to the loss of signal near the boundaries in the LDV technique.

We find that the direct numerical simulations (DNS) of Yeo & Maxey [36] follow our experimental measurements. The shape of concentration profiles are fairly similar. Moreover, the maximum concentration at the channel center is below ϕ_m for ϕ_b = 0.2 and 0.3, and of same order of magnitude as in our experiments. For ϕ_b = 0.4, ϕ_m is reached at the middle in both our experiments and the simulations. It is noteworthy to mention that Yeo & Maxey [36] have studied the flow for three different confinement ratios (ratio between the channel width to the particle diameter $\hat{D}/\hat{d}_p$). The numerical results show the particle layering close to the walls for $\hat{D}/\hat{d}_p$ = 18 and $\hat{D}/\hat{d}_p$ = 24. We have recently addressed the layering effect and explained it is associated with the discrete effect and crystallization of the particles close to the boundaries. We have shown that the particle layering does not affect the fully-developed concentration profiles averaged over a broader neighborhood [10].

Our experimental observations are not entirely consistent with the SBM framework, particularly as we approach the channel's center for $\bar{\phi}_b \lessapprox 0.3$. The model results in cusps forming in the central regions where the solid volume fraction approaches ϕ_m. Nott and Brady [30] proposed a resolution for resolving the cusp via including the nonlocal effects. They suggested adding an equation for the granular temperature to the system of the equations. The diffusion of the granular temperature results in a blunter solid volume fraction profile and removal of the cusp. Nonetheless, the discrepancy between the prediction of SBM and our experimental data for $\bar{\phi}_b \lessapprox 0.3$ in the central region is more than the value of nonlocal's resolution given in [30].

The novelty of our setup enables us to measure the axial development of the solid volume fraction experimentally for the first time. We report the particle concentration profiles at different locations as we march along with the flow, x direction. Figures 6 (a)-(e) show the results of our experimental observations for different values of $\bar{\phi}_b$.

The particle migration can be clearly observed by the increase in particle volume fraction ϕ at the center of the channel ($y = 0$) and its decrease near the edges ($y = 0.4$). Furthermore, we observe that the migration occurs faster at larger bulk volume fraction $\bar{\phi}_b$, i.e, the particle concentration reaches its fully-developed state at a smaller length along the flow direction x. The reduction of steady-state length scale by bulk volume fraction enhancement is in agreement with the SBM framework [30] and can be explained via equation (11). Indeed, a balance of the right-hand side and left-hand side of this equation implies that the fully-developed length, x, scales inversely with $(f(\phi)/\phi)) \times \Sigma_p(\phi)$. The latter is an increasing function of $\bar{\phi}_b$ resulting in a shorter fully-developed length as $\bar{\phi}_b$ increases.

The predictions of the the nearly one-dimensional equation (11) with the Morris and Boulay [43] laws are presented in Figures 6 (f)-(j) for the same x and $\bar{\phi}_b$ values as for the experimental data of Figures 6 (a)-(e). The shape of the curve and their evolution with x are in fair agreement with the data. We note that the central region's size where most of the particles accumulate is of the same order of magnitude in both the experiments and the model. This region grows with $\bar{\phi}_b$. As noted above, the main discrepancy is that the volume fraction always reaches ϕ_m at the center in the model, which is not the case at low $\bar{\phi}_b$ in experiments.

To better characterize the axial development of the volume fraction profiles, we compute the average of $\phi - \phi_{initial}$ over the central region (from $y = 0$ to $y = 0.10$). Fig. 7 shows the experimental data and solution of equation (11) follow the same shape. However, the migration is slower in the experiments for $\phi_b = 0.5$. This plot allows us to provide a crude estimate of the order of magnitude of x for the fully developed state which is found to be of order 0.8 for $\bar{\phi}_b = 0.1$, of order 0.5 for $\bar{\phi}_b = 0.2$, $\bar{\phi}_b = 0.3$, and $\bar{\phi}_b = 0.4$, and of order 0.4 for $\bar{\phi}_b = 0.5$. It is impossible to report more accurate values as it would require scanning the whole channel and an extremely long time to run the experiment.

The steady-state data can be presented differently for the purpose of the comparison with constitutive equations. As pointed out by Ramachandran & Leighton [52], the dimensionless gradient $y(d\phi/dy)$ in the fully developed state should be a function only of the concentration. Figure 8 shows the comparison between the present work and the SBM prediction (rheological law of Morris & Boulay [43]) of the dimensionless concentration gradient in the channel flow. The results show that the dimensionless gradient is only a function of concentration. All data fall on a master curve, except for those at the center of the channel. In this region, the data show an abrupt jump to zero. Such a trend points to the breakdown of the continuum modeling in the central region. This plot also confirms the fair agreement with the Morris and Boulay model.

Finally, we discuss the velocity profiles. Figure 9 presents the measurements of the particle phase velocity close to the outlet for different bulk volume fractions. We normalize the velocity profiles with the value of the velocity at the center for a Newtonian fluid. u_p is the particle phase velocity that is measured from the experiment, and u_N is

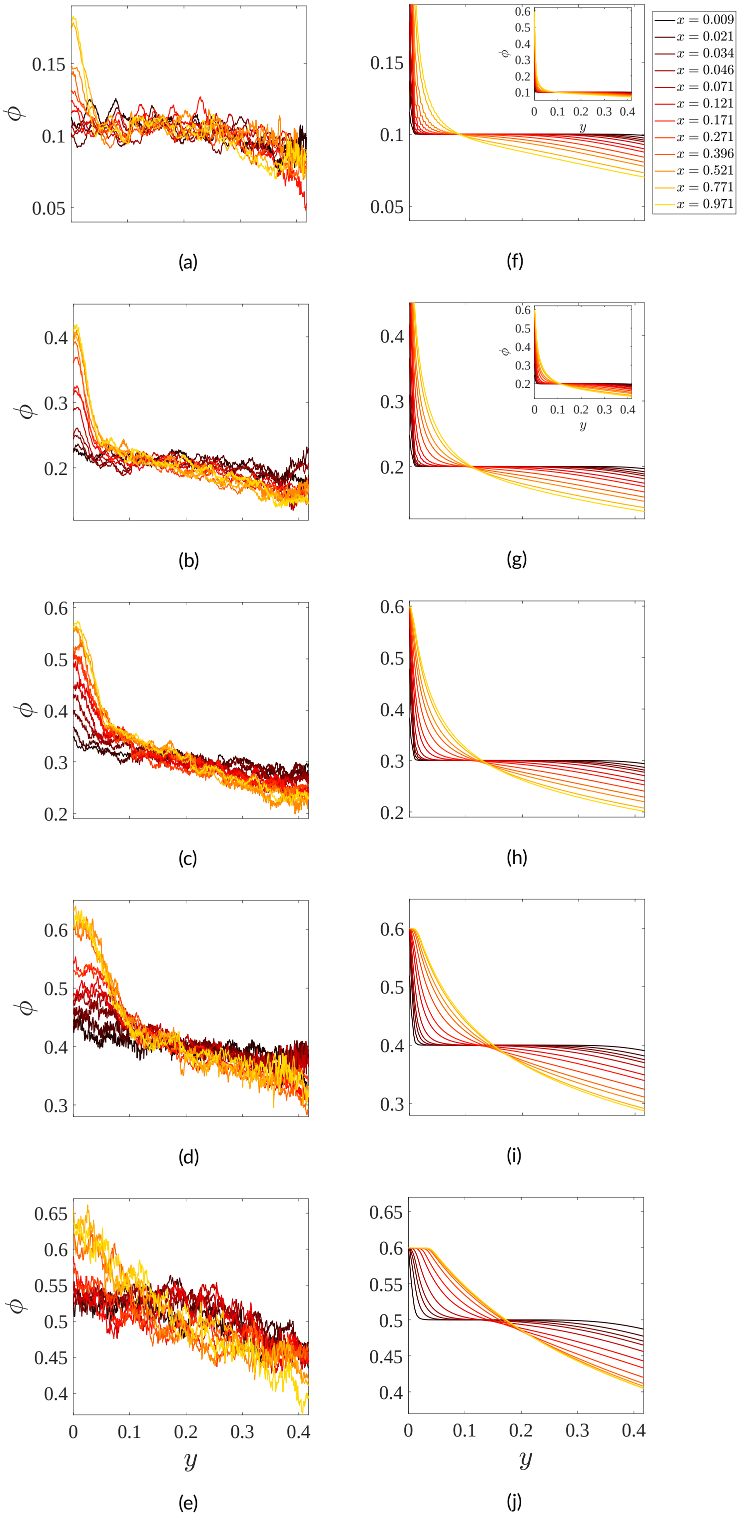

FIGURE 6 Axial evolution of the particle concentration for present work at different bulk volume fractions of (a) $\bar{\phi}_b$ = 0.1, (b) $\bar{\phi}_b$ = 0.2, (c) $\bar{\phi}_b$ = 0.3, (d) $\bar{\phi}_b$ = 0.4, (e) $\bar{\phi}_b$ = 0.5; Evolution of the particle concentration for the two-dimensional SBM prediction with the rheological laws of Morris & Boulay (1999) [43] at different bulk volume fractions of (f) $\bar{\phi}_b$ = 0.1, (g) $\bar{\phi}_b$ = 0.2, (h) $\bar{\phi}_b$ = 0.3, (i) $\bar{\phi}_b$ = 0.4, (j) $\bar{\phi}_b$ = 0.5.

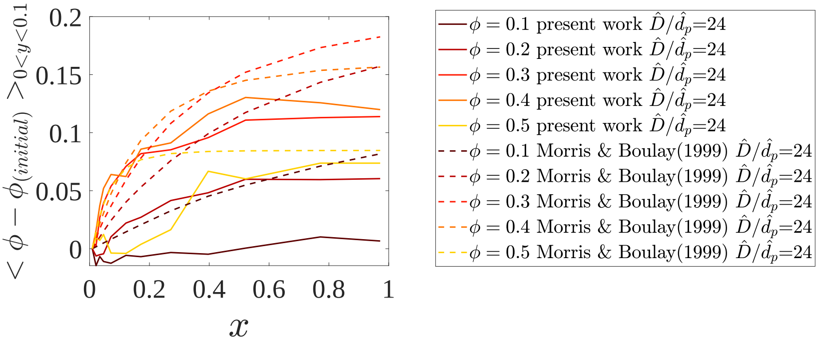

FIGURE 7 The spatially averaged $\phi - \phi_{initial}$ from $y = 0$ to $y = 0.10$ vs x.

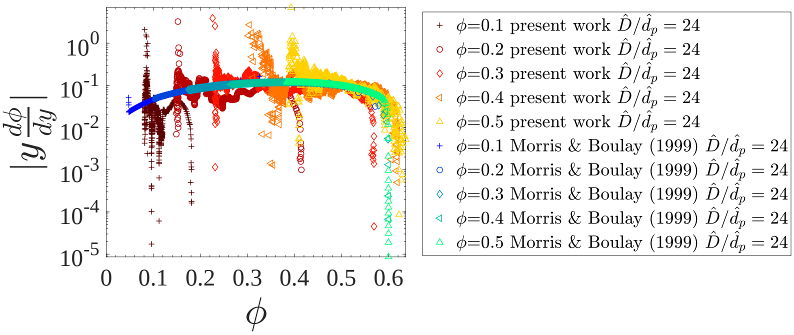

FIGURE 8 A comparison between the present work and the 2D SBM prediction (rheological law of Morris & Boulay [43]) for the dimensionless concentration gradient in the channel flow.

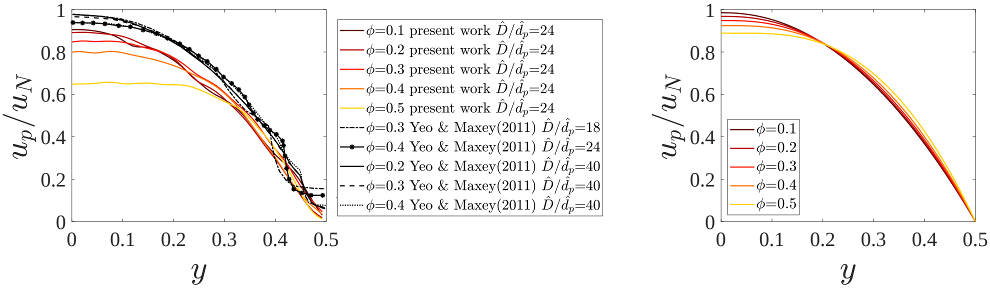

(a)

(b)

FIGURE 9 (a) The particle phase velocity at the end of the channel normalized by theoretical velocity for Newtonian fluid at the center with the same condition at different bulk volume fractions $\bar{\phi}_b$ for present work and simulations of Yeo & Maxey [36]; (b) The steady-state suspension velocity at different bulk volume fractions $\bar{\phi}_b$ for SBM prediction with rheological law of Morris & Boulay (1999) $\hat{D}/\hat{d}_p = 24$ [43].

the theoretical velocity for Newtonian fluid at the center of the channel with the same condition. The results show that the velocity evolves toward a blunt profile as we increase the bulk volume fractions $\bar{\phi}_b$. This trend is similar to the prediction of the SBM for the suspension velocity profile (see Figure 9 (b)). As far as the particle phase velocity is concerned, we have compare our results with that of Yeo & Maxey [36]. Figure 9 (a) shows that the experimental velocity profiles have smaller magnitudes compare to those computed from the Numerical simulations.

Here we show the consistency between the steady-state volume fraction profiles, the steady-state velocity profiles, and the continuum modeling. To this end, we have computed the velocity profiles from the measurements of $\phi(y)$ using $\eta(\phi)$ from the rheological law of Morris and Boulay [43]. In the central plane of the channel, suspension shear stress at steady-state is $\tau \propto y$. Therefore, we can compute the shear rate as $\dot{\gamma}(y) = \tau(y)/\eta(\phi(y)) \propto y/\eta(\phi(y))$. Then, the velocity profile can be computed by integrating the shear rate. In the absence of a pressure drop measurement, the velocity can then be known only up to a constant. We match the computed velocity at the center with our PIV measurements. Figure 10 shows a good agreement between these two velocity profiles. This agreement implies the viscosity function $\eta(\phi)$ chosen to compute the velocity profile from ϕ measurements accounts correctly for the material behavior.

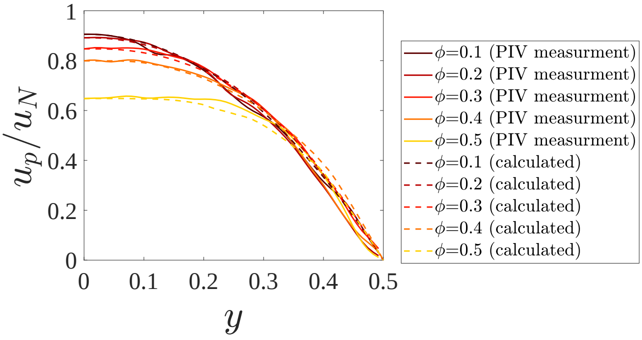

FIGURE 10 The particle phase velocity at the end of the channel normalized by theoretical velocity for Newtonian fluid at the center with the same condition at different bulk volume fractions $\bar{\phi}_b$ obtained from PIV measurements and the calculated velocity from the distribution of solid volume fractions.

5 | SUMMARY

A high precision rectangular channel is designed to experimentally study the evolution of the solid volume fraction in fracturing flows. We conducted experiments to study the shear-induced migration of rigid spheres in a Newtonian fluid, in the Stokesian regime. We adopted a highly-resolved index-matching technique and particle image velocimetry to calculate the solid volume fraction profiles and the particle phase velocity, respectively. Well-controlled experiments were performed for a wide range of bulk volume fractions ranging from 0.1 to 0.5 to cover the whole range of dilute to dense suspension flows. Fully-developed concentration profiles , along with the axial developments and migration dynamics were analyzed and compared with the existing experimental and computational studies.

We find that the maximum particle volume fraction, which occurs at the channel centerline, increases with the bulk volume fraction and eventually gets saturated to a value of 0.6 for $\bar{\phi}_b \gtrapprox 0.3$. Overall, the SBM with the Morris and Boulay law provides a fair description of the migration profiles and of their axial development. However, there exist discrepancies between our experimental data and the prediction of the SBM framework. One difference is that the SBM predicts that the local particle concentration reaches the maximum packing fraction ϕ_m at the channel centerline regardless of the value of the bulk volume fraction.

Besides, we compared some of our experimental data with the available experimental and computational results. We showed that the concentration profiles shapes resulted from fully three-dimensional numerical simulations performed in a channel flow by Yeo & Maxey [36] are fairly similar to our results, and the maximum concentration at the channel center is of same order. In these well-resolved simulations, the authors considered the discrete effect resulting from the confinement and finite-size of the particles, which is more pronounced at the larger bulk volume fraction. Here, we tried to minimize these effects by performing our experiments for the largest possible confinement ratio, $\hat{D}/\hat{d}_p = 24$. Although there exist particle layerings close to the boundaries, we could not measure it in this work due to the low signal-to-noise-ratio.

Furthermore, we find that our measurements are in qualitative agreement with the previous experimental study of Koh *et al.* [21] and Lyon & Leal [22] in the core region (far from the center and solid walls). Nonetheless, their fully-developed particle volume fraction measurements deviate from ours in the vicinity of walls and near the channel centerline. It might be due to the signal loss in the LDV technique close to the channel walls as the solid volume fraction decreases. In Koh's experiments [21], the particle size and channel length were kept fixed and the confinement ratio ($\hat{D}/\hat{d}_p$) was varied by changing the channel width.

The unique feature of our setup in resembling a long and thin fracture allows us to provide data on the axial development of the solid volume fraction for both dilute and dense flow of suspensions. We showed the evolution of ϕ along the flow direction x, i.e., from the inlet to the outlet of the channel.

Finally, we have performed a PIV analysis to measure the particle phase velocity. We observed that the particle phase velocity profiles evolve from a parabolic shape to a plug shape by increasing the bulk volume fraction $\bar{\phi}_b$. It is expected as the solution to the velocity profile is coupled to the solid volume fraction exhibiting a blunter profile, in the core region of the channel flow, for larger values of $\bar{\phi}_b$. Also, we observed a good agreement between the measured velocity profiles from PIV with the velocity profiles calculated from the measured concentration profiles.

The highly-resolved experimental data presented in this study provids an insight into understanding the dispersion of solids in fracturing flows of petroleum industries. In the near future, we will provide more experimental data on the effect of boundaries, crystallization, dynamics, solid inhomogeneities, and non-Newtonian interstitial fluid. Our experimental effort along with the recent work of other researchers in the field e.g., [10, 16, 19, 20, 31] may provide a basis for improving the continuum model frameworks explaining the flows of non-Brownian suspensions.

acknowledgements

This work was supported by the National Science Foundation (NSF) (Grant No. CBET-1554044-CAREER) and ACS PRF (Grant no. 55661-DNI9) via the research awards (S.H.) and the University of Bordeaux Idex (Grant no. ANR-10–IDEX-03-02). The authors thank Randy Mulford, Zachery Tucker, and Kane Pickrel for their assistance in machining the setup and also John Satterfield and Jarad Baldridge for their help in performing the experiments. The authors also thank Professor Frederic Blanc and Professor Bernard Pouligny for fruitful discussions and guidance on the optics and image analysis. Moreover, the authors thank Professor Amir Farnoud for providing circulating water bath facility.

references

[1] EIA U. Hydraulic fracturing accounts for about half of current US crude oil production. March 2016;15:2016.

[2] EIA U, Hydraulically fractured wells provide two-thirds of US natural gas production. May; 2016.

[3] Gillard MR, Medvedev OO, Hosein PR, Medvedev A, Peñacorada F, d'Huteau E, et al. A new approach to generating fracture conductivity. In: SPE Annual Technical Conference and Exhibition Society of Petroleum Engineers; 2010. .

[4] Huang B, Liu C, Fu J, Guan H. Hydraulic fracturing after water pressure control blasting for increased fracturing. International Journal of Rock Mechanics and Mining Sciences 2011;48(6):976–983.

[5] Hormozi S, Frigaard I. Dispersion of solids in fracturing flows of yield stress fluids. Journal of Fluid Mechanics 2017;830:93–137.

[6] Guazzelli E, Pouliquen O. Rheology of dense granular suspensions. Journal of Fluid Mechanics 2018;852.

[7] Guazzelli E, Morris JF. A physical introduction to suspension dynamics, vol. 45. Cambridge University Press; 2011.

[8] Leighton D, Acrivos A. The shear-induced migration of particles in concentrated suspensions. Journal of Fluid Mechanics 1987;181:415–439.

[9] Phillips RJ, Armstrong RC, Brown RA, Graham AL, Abbott JR. A constitutive equation for concentrated suspensions that accounts for shear-induced particle migration. Physics of Fluids A: Fluid Dynamics 1992;4(1):30–40.

[10] Sarabian M, Firouznia M, Metzger B, Hormozi S. Fully developed and transient concentration profiles of particulate suspensions sheared in a cylindrical Couette cell. Journal of Fluid Mechanics 2019;862:659–671.

[11] Gadala-Maria F, Acrivos A. Shear-induced structure in a concentrated suspension of solid spheres. Journal of Rheology 1980;24(6):799–814.

[12] Abbott J, Tetlow N, Graham A, Altobelli S, Fukushima E, Mondy L, et al. Experimental observations of particle migration in concentrated suspensions: Couette flow. Journal of rheology 1991;35(5):773–795.

[13] Chow AW, Sinton SW, Iwamiya JH, Stephens TS. Shear-induced particle migration in Couette and parallel-plate viscometers: NMR imaging and stress measurements. Physics of Fluids 1994;6(8):2561–2576.

[14] Ovarlez G, Bertrand F, Rodts S. Local determination of the constitutive law of a dense suspension of noncolloidal particles through magnetic resonance imaging. Journal of rheology 2006;50(3):259–292.

[15] Bricker JM, Butler JE. Oscillatory shear of suspensions of noncolloidal particles. Journal of rheology 2006;50(5):711–728.

[16] Saint-Michel B, Manneville S, Meeker S, Ovarlez G, Bodiguel H. X-ray radiography of viscous resuspension. Physics of Fluids 2019;31(10):103301.

[17] Karnis A, Goldsmith H, Mason S. The kinetics of flowing dispersions: I. Concentrated suspensions of rigid particles. Journal of Colloid and Interface Science 1966;22(6):531–553.

[18] Hampton R, Mammoli A, Graham A, Tetlow N, Altobelli S. Migration of particles undergoing pressure-driven flow in a circular conduit. Journal of Rheology 1997;41(3):621–640.

[19] Oh S, Song Yq, Garagash DI, Lecampion B, Desroches J. Pressure-driven suspension flow near jamming. Physical review letters 2015;114(8):088301.

[20] Snook B, Butler JE, Guazzelli É. Dynamics of shear-induced migration of spherical particles in oscillatory pipe flow. Journal of Fluid Mechanics 2016;786:128–153.

[21] Koh CJ, Hookham P, Leal LG. An experimental investigation of concentrated suspension flows in a rectangular channel. Journal of Fluid Mechanics 1994;266:1–32.

[22] Lyon M, Leal L. An experimental study of the motion of concentrated suspensions in two-dimensional channel flow. Part 1. Monodisperse systems. Journal of Fluid Mechanics 1998;363:25–56.

[23] Deshpande KV, Shapley NC. Particle migration in oscillatory torsional flows of concentrated suspensions. Journal of Rheology 2010;54(3):663–686.

[24] Sarabian M, Rosti ME, Brandt L, Hormozi S. Numerical simulations of a sphere settling in simple shear flows of yield stress fluids. Journal of Fluid Mechanics 2020;896.

[25] Izbassarov D, Rosti ME, Ardekani MN, Sarabian M, Hormozi S, Brandt L, et al. Computational modeling of multiphase elastoviscoplastic flows. arXiv preprint arXiv:180309563 2018;.

[26] Alghalibi D, Lashgari I, Brandt L, Hormozi S. Interface-resolved simulations of particle suspensions in Newtonian, shear thinning and shear thickening carrier fluids. Journal of Fluid Mechanics 2018;852:329–357.

[27] Izbassarov D, Rosti ME, Ardekani MN, Sarabian M, Hormozi S, Brandt L, et al. Computational modeling of multiphase viscoelastic and elastoviscoplastic flows. International Journal for Numerical Methods in Fluids 2018;88(12):521–543.

[28] Brady JF, Morris JF. Microstructure of strongly sheared suspensions and its impact on rheology and diffusion. Journal of Fluid Mechanics 1997;348:103–139.

[29] Morris J, Brady J. Pressure-driven flow of a suspension: Buoyancy effects. International journal of multiphase flow 1998;24(1):105–130.

[30] Nott PR, Brady JF. Pressure-driven flow of suspensions: simulation and theory. Journal of Fluid Mechanics 1994;275:157–199.

[31] d'Ambrosio E, Blanc F, Lemaire E. Viscous resuspension of non-Brownian particles: determination of the concentration profiles and particle normal stresses. arXiv preprint arXiv:190701793 2019;.

[32] Deboeuf A, Gauthier G, Martin J, Yurkovetsky Y, Morris JF. Particle pressure in a sheared suspension: A bridge from osmosis to granular dilatancy. Physical review letters 2009;102(10):108301.

[33] Dbouk T, Lobry L, Lemaire E. Normal stresses in concentrated non-Brownian suspensions. Journal of Fluid Mechanics 2013;715:239–272.

[34] Boyer F, Pouliquen O, Guazzelli É. Dense suspensions in rotating-rod flows: normal stresses and particle migration. Journal of Fluid Mechanics 2011;686:5–25.

[35] Boyer F, Guazzelli É, Pouliquen O. Unifying suspension and granular rheology. Physical Review Letters 2011;107(18):188301.

[36] Yeo K, Maxey MR. Numerical simulations of concentrated suspensions of monodisperse particles in a Poiseuille flow. Journal of fluid mechanics 2011;682:491–518.

[37] Gholami M, Rashedi A, Lenoir N, Hautemayou D, Ovarlez G, Hormozi S. Time-resolved 2D concentration maps in flowing suspensions using X-ray. Journal of Rheology 2018;62(4):955–974.

[38] Rashedi A, Ovarlez G, Hormozi S. Engineered transparent emulsion to optically study particulate flows in yield stress fluids. Experiments in Fluids 2020;61(2):1–13.

[39] Ovarlez G, Mahaut F, Deboeuf S, Lenoir N, Hormozi S, Chateau X. Flows of suspensions of particles in yield stress fluids. Journal of rheology 2015;59(6):1449–1486.

[40] Dagois-Bohy S, Hormozi S, Guazzelli É, Pouliquen O. Rheology of dense suspensions of non-colloidal spheres in yield-stress fluids. Journal of Fluid Mechanics 2015;776.

[41] Firouznia M, Metzger B, Ovarlez G, Hormozi S. The interaction of two spherical particles in simple-shear flows of yield stress fluids. Journal of Non-Newtonian Fluid Mechanics 2018;255:19–38.

[42] Miller RM, Morris JF. Normal stress-driven migration and axial development in pressure-driven flow of concentrated suspensions. Journal of non-newtonian fluid mechanics 2006;135(2-3):149–165.

[43] Morris JF, Boulay F. Curvilinear flows of noncolloidal suspensions: The role of normal stresses. Journal of rheology 1999;43(5):1213–1237.

[44] Lhuillier D. Migration of rigid particles in non-Brownian viscous suspensions. Physics of Fluids 2009;21(2):023302.

[45] Nott PR, Guazzelli E, Pouliquen O. The suspension balance model revisited. Physics of Fluids 2011;23(4):043304.

[46] Pham PN. Origin of shear-induced diffusion in particulate suspensions: crucial role of solid contacts between particles. PhD thesis, Aix-Marseille; 2016.

[47] Diemunsch G, Prenel J. A compact light sheet generator for flow visualizations. Optics & Laser Technology 1987;19(3):141–144.

[48] Prenel J, Jeudy M. A new versatile laser sheet generator for flow visualization. Optics & Laser Technology 1998;30(8):533–538.

[49] Li CH, Lee C. Minimum cross entropy thresholding. Pattern recognition 1993;26(4):617–625.

[50] Schneider CA, Rasband WS, Eliceiri KW. NIH Image to ImageJ: 25 years of image analysis. Nature methods 2012;9(7):671–675.

[51] Sveen JK. An introduction to MatPIV v. 1.6. 1. Preprint series Mechanics and Applied Mathematics http://urn nb no/URN: NBN: no-23418 2004;.

[52] Ramachandran A, T LEIGHTON D. The influence of secondary flows induced by normal stress differences on the shear-induced migration of particles in concentrated suspensions. Journal of Fluid Mechanics 2008;603:207.

[53] Sinton SW, Chow AW. NMR flow imaging of fluids and solid suspensions in Poiseuille flow. Journal of Rheology 1991;35(5):735–772.